Enhanced Anticancer Property of Polyphenol-Assisted Biogenic AuNPs/RGO Nanocomposites in Triple-Negative Breast Cancer Cells

R. Prasannadevi[1], T. Radhiga[2], N. Rajendra Prasad[2,], S. Dhanapandian[1] and N. Krishnakumar[1,3,*,]

[1]Department of Physics, Annamalai University, Annamalainagar-608002, India
[2]Department of Biochemistry and Biotechnology, Annamalai University, Annamalainagar-608002, India
[3]School of Physics, Madurai Kamaraj University, Madurai-625021, India

*Corresponding author: E-mail: nskumarphyamu@gmail.com

The bio-inspired nanocomposites developed from reduced graphene oxide (RGO) and gold nanoparticles (AuNPs) might be of great significance due to their exceptional physico-chemical properties. In the present work, the AuNPs/RGO nanocomposites were prepared by a green-synthesis approach using grape seed proanthocyanidin (GSP), which acts as a natural reducing and stabilizing agent. The simultaneous biosynthesis of RGO nanosheets from graphene oxide (GO) and AuNPs from chloroauric acid ions by GSP leads to the development of AuNPs/RGO nanocomposites, which were further confirmed by various analytical techniques. The analyses of the observed outcomes confirm the removal of oxygen containing moieties during the transformation process of GO to RGO. Further, AuNPs were decorated orderly on both sides of the RGO nanosheet surface with an average particle size of ~ 35 nm. The MTT-based cytotoxicity assay revealed the enhanced anticancer activity of the prepared AuNPs/RGO nanocomposites (IC_{50} = 15.6 µg/mL) against triple-negative breast cancer cells when compared to either AuNPs or RGO treatment alone. Moreover, enhanced ROS levels and subsequent alteration in mitochondrial membrane potential ($\Delta\psi$m) with nuclear fragmentation and apoptotic features were observed in AuNPs/RGO nanocomposites treated cells. This could be due to the synergistic effect of AuNPs/RGO in the triple-negative breast cancer cells.

Keywords: Gold nanoparticles, Reduced graphene oxide, Nanocomposites, Grape seed proanthocyanidin, Breast cancer, Cytotoxicity.

INTRODUCTION

Breast cancer is one of the leading cause of death for women across the globe. The prevalence of breast cancer rate is on the rise due to a sedentary lifestyle and hormonal imbalance [1]. Triple-negative breast cancer is an aggressive form of breast cancer associated with a poor prognosis [2]. The triple-negative breast tumor tissues have been identified with estrogen and progesterone receptors with excess HER-2 receptors [3]. Neo-adjuvant chemotherapy is considered a preferred treatment method for triple-negative breast cancer as it preserves breast tissues from surgical resection [4]. Clinical anticancer drugs including 5-fluorouracil, paclitaxel, gemcitabine, bleomycin, carboplatin and doxorubicin have been used to improve the survival rate of breast cancer patients [5-9]. Both neoadjuvant chemotherapy and adjuvant chemotherapy with surgery possess serious adverse effects in normal tissues, which further develop

clinical multidrug resistance (MDR) [10]. Besides systemic toxicity, these conventional anticancer agents show low bio-availability, poor stability and impaired target specificity. Therefore, there is a need to establish novel therapeutic strategies with high specificity, increased efficacy and minimum adverse effects.

The advancement of multifunctional nanomaterials with structural versatility, controlled size, good biocompatibility and surface functional moieties have garnered tremendous attention for enhanced therapeutic benefits [11]. Recently, two-dimensional (2D) nanomaterials have gained significant attention in cancer therapeutics due to their unique physico-chemical properties [12-14]. Graphene is a well-studied 2D material with a honeycomb structure of sp^2 hybridized carbon atoms [15]. Because of its exceptional and distinct physical and chemical properties, graphene has attracted significant attention in the field of biomedicine and bioengineering [16-18]. Graphene and

its derivatives, notably reduced graphene oxides (RGO), have been integrated with drugs, antibodies and other nanomaterials for drug delivery applications [19,20]. The combination of graphene nanosheets with other nanomaterials has been considered as nanocomposites that might possess a higher specific surface area with synergistic biological effects. However, owing to the strong π-π stacking and the strong van der Waals forces, the graphene sheets form severe agglomeration and restack into layered graphitic structures. This hydrophobicity limits graphene and graphene oxides to be explored in biomedical applications. Hence, there has been a growing interest to incorporate metallic nanoparticles into/onto GO or RGO, which prevents them from undergoing restacking. These conjugated graphene-metal based nanocomposites exhibit superior physico-chemical properties to achieve the desired therapeutic outcome [21]. It has been found that the integration of 2D nanomaterials with various noble metal nanostructures (Au, Ag, Pd, Pt and Cu) augment the therapeutic potentials due to synergistic effects [21-24]. Comparatively, gold nanoparticles (AuNPs) have mainly been explored for anticancer applications owing to their high drug-loading ability, excellent biocompatibility and biodegradation property [21,24]. Therefore, integrating graphene nanosheets with AuNPs might achieve synergistic performance against an aggressive form of cancer cells.

The synthesis of nanomaterials with the existing physical and chemical reduction methods requires expensive toxic reducing agents and requires high-end instrumentations [25]. Recently, sustainable green-chemistry based biogenic approaches were employed to develop nanocomposites for biological applications [26,27]. Graphene-based nanocomposites were effectively synthesized using plant extracts, microorganisms, organic acids and biomass sources [28-30]. However, most of the existing green chemistry approaches suffer from long reaction time, formation of heterogeneous shapes and sizes, particle aggregation, non-reproducibility and energy consumptions. Moreover, the reduction and surface functionalization mechanisms were not effective in plant crude extracts' mediated nanofabrication [31]. Instead of crude plant extracts, plant derived polyphenolic flavonoids are considered a promising reducing/stabilizing agents due to their effective reduction potential [32]. Different plant derived flavonoids were found to generate homogeneous nanomaterials with uniform shapes and sizes through a reductive synthesis mechanism [27,31,33]. However, there is a paucity in the literature pertaining to the simultaneous biosynthesis of AuNPs/RGO nanocomposites using flavonoids as a reducing/stabilizing agent.

Proanthocyanidins (flavan-3-ol) are the naturally available polyphenolic compounds present in flowers, vegetables, fruits, seeds, nuts and barks. Grape seed is an abundant source of proanthocyanidin, which exhibits superior anticancer effects against various human cancer subtypes. Preclinical studies show that grape seed proanthocyanidin (GSP) induces cancer cell apoptosis through ROS generation [34]. Hence, in the present study, an attempt has been made to explore the novel and environmentally benign GSP as a reducing and stabilizing agent for the simultaneous synthesis of AuNPs/RGO nanocomposites for anticancer applications. The obtained AuNPs/RGO nano-

composites were subsequently characterized by UV-visible absorption, FT-IR, TEM, SEM-EDX and zeta potential analysis. Furthermore, the anticancer potential of prepared AuNPs/RGO nanocomposites was tested against triple-negative breast cancer (MDA-MB- 231) cell lines.

EXPERIMENTAL

Graphite powder (100 mesh), conc. sulfuric acid (98%), potassium permanganate (99%), hydrogen peroxide (35%), sodium nitrate (99%), hydrogen chloride (36.46%) were procured from S.D. Fine Chemicals Company, India. Hydrogen tetra-chloroaureate(III) hydrate $HAuCl_4 \cdot 3H_2O$ (99.9%), Dulbecco's modified Eagle's medium (DMEM), 2′,7′-dichlorofluorescein diacetate (DCFH-DA), 3-(4,5-dimethyl-2-thiazolyl)-2,5-diphenyl-2*H*-tetrazolium bromide (MTT), heat-inactivated fetal calf serum (FCS) and antibiotics (penicillin and streptomycin) were procured from Sigma-Aldrich Chemical Pvt. Ltd, India and used as received. Acridine orange, ethidium bromide, Rhodamine 123 (Rh-123) and phosphate buffered saline (PBS) were bought from Himedia, India. Grape seed proanthocyanidin (GSP) (purity < 96%, Lot no. G050412) was obtained from Tianjin Jianfeng Natural Product R&D Co. Ltd. (China). Other chemicals were of analytical grade obtained from local firms.

Synthesis of graphene oxide (GO): Graphene oxide (GO) was synthesized following the modified Hummer's method from synthetic graphite powder [29,35]. Briefly, graphite powder (1 g), sodium nitrate (0.0117 mol) and conc. H_2SO_4 (0.0102 mol) were added together and the resultant solution was kept in an ice bath at 0 ºC. Further, $KMnO_4$ (0.0379 mol) was added slowly to the cooled homogeneous mixture with vigorous stirring conditions below 5 ºC for 4 h. After incubation at 35 ºC for 20 min, the whole solution was diluted with 133 mL of deionized water. The suspension was stirred for 2 h at 98 ºC. After that 225 mL excess deionized water was added to the solution and stirred for 30 min followed by 35 mL H_2O_2 treated with a deep brown mixture of dispersion turned brilliant yellow. The resultant mixture was filtered, washed with deionized water and diluted HCl followed by centrifugation at 3500 rpm to neutralize pH and remove metal ions from oxidized graphene [36]. Finally, the obtained product was oven-dried at 60 ºC for 8 h.

Synthesis of reduced graphene oxide (RGO): The aqueous dispersion of GO (40 mL, 1 mg/mL) was sonicated for 30 min. Then, 0.12 mg of GSP was added to the homogenous suspension of GO by magnetic stirring for 5 min at room temperature. The pH of the homogenous suspension was adjusted to ~ 10 with the required amount of NH_3 solution. Then, the reaction mixture was continually stirred up for 10 h at 95 ºC under the reflux bath. The resultant suspension was centrifuged at 3500 rpm and washed with distilled water to remove the unreacted GSP residue. The obtained solid was dried in the oven and collected the reduced graphene oxide (RGO) powder.

Synthesis of gold nanoparticles (AuNPs): Chloroauric acid ($HAuCl_4$) was used as the precursor material for synthesizing gold nanoparticles (AuNPs). In brief, aqueous AuNPs solution was obtained by adding 0.10 mM of chloroauric acid ($HAuCl_4$) solution with 100 mL distilled water. Then, 3.6 mg

of GSP was dissolved in 30 mL of distilled water and used as a stock solution. The pH of the solution was adjusted to ~7 by using NH_3 solution. A $HAuCl_4$ solution (10 mL) and stock solution (7 mL) was blended in a beaker and the reaction mixture was heated to 80 °C for 15 min. Finally, the colour of reaction mixture turned ruby red, which confirmed the reduction of Au^+ ions into AuNPs [37].

Synthesis of AuNPs/RGO nanocomposites: In a conical flask, the obtained RGO (35 mg) powder was dissolved in 10 mL of deionized water followed by sonication for 30 min. Then, 190 mL of aqueous $HAuCl_4$ solution (0.20 mM) was added to the prepared RGO solution and magnetic stirred for 15 min followed by the addition of 140 mL GSP stock solution [ratio of AuNPs/GSP (10:7)] and mixed for 10 min at room temperature. Subsequently, the reaction mixture was kept in a water bath at 80 °C and stirred for 8 h. The resultant dispersion was washed with distilled water followed by the centrifugation in order to remove any residuals and dried in an oven at 60 °C.

Characterization: The synthesized nanocomposites have been characterized by UV-visible absorption spectroscopy (Shimadzu-UV 1800), high-resolution transmission electron microscopy (Jeol/JEM 2100), Fourier transforms infrared (FT-IR) spectroscopy (PerkinElmer RX1), energy-dispersive X-ray spectroscopy (EDS, Jeol-JSM-IT 200) and zeta size analyzer (Malvern Zetasizer Nano-ZS).

Cell culture: Human breast cancer cell lines (MDA-MB-231) were procured from the National Centre for Cell Science (NCCS), Pune, India whereas the MDA-MB-231 cells were maintained in DMEM containing 10% FCS, 100 µg/mL of streptomycin and 100 U/mL of penicillin at 37 °C in 95 % humidified atmosphere air and 5% CO_2 incubator.

Cytotoxicity assay: The MTT assay is an accurate and simple colorimetric non-radioactive assay to determine the activity of living (healthy) cells through the reduction of tetrazolium salt. The MDA-MB-231 cells at the density of 1,00,000 viable cells per well were seeded in 96 well culture plates and kept incubated overnight before treatment. After overnight incubation, GSP, GO, RGO, AuNPs and AuNPs/RGO nanocomposites were added to the culture media (1.95 to 1000 µg mL^{-1}) and again incubated for 24 h in the presence of 95% O_2 and 5 % CO_2 at 37 °C. Then, MTT solution (100 µL) was added to each well and incubated for another 4 h. Subsequently, the supernatant was removed carefully with the addition of DMSO to dissolve the violet formazan crystals. The optical absorbance was recorded at 450 nm using the microplate multi-mode reader (Tecan Multimode Reader, Austria). The half-maximal inhibitory concentration (IC_{50}) values were obtained from the microplate reader and its optimum dosage was used for further study. The cytotoxicity effect was estimated using triplicate cultures and the mean and standard deviation was calculated. The percentage viability was calculated by using the following formula:

$$\text{Viability (\%)} = \frac{A - B}{A} \times 100$$

where A = Mean optical density of untreated cells (control), B = Mean optical density of treated cells.

Measurement of intracellular reactive oxygen species (ROS): The intracellular ROS levels were measured using 2′,7′-dichlorofluorescein diacetate (DCFH-DA) dye to penetrate the intracellular matrix of cells. The intracellularly trapped DCFH has been oxidized by reactive oxygen species (ROS), which generates high green fluorescence emitting oxidized DCF. The MDA-MB-231 cells were exposed to the IC_{50} concentrations of GSP, GO, RGO, AuNPs and AuNPs/RGO nanocomposites in 6 well plates (2×10^6 cells/well) and incubated for 24 h. The cells were then exposed to 10 µM DCFH-DA and incubated for 30 min at 37 °C. PBS was used to wash the cells twice to eliminate the excess amount of dye. The DCF fluorescence intensity was measured using the Tecan microplate multimode reader (Excitation-485 nm; Emission-530 nm). DCF fluorescence was observed by a Floid cell imaging station (Invitrogen, USA).

Analysis of mitochondrial membrane potential (MMP, Δψm): The modification of mitochondrial membrane potential (Δψm) is the critical event during drug-induced apoptosis. The loss of mitochondrial membrane potential (Δψm) in MDA-MB-231cells was assessed using rhodamine 123 stainings. In brief, theMDA-MB-231 cells were cultured in 6 well plates at a density of (1×10^4 cells/well) and incubated with IC_{50} concentrations of GSP, GO, RGO, AuNPs and AuNPs/RGO nanocomposites for 24 h at 37 °C. The cells were then stained with fluorescent Rhodamine-123 dye for another 30 min. The excess stain was eliminated by washing with PBS and the treated cells were visualized under a floid cell imaging station (Invitrogen, USA).

Apoptotic morphological changes by acridine orange (AO)/ethidium bromide (EB) dual staining method: The induction of apoptosis by GSP, GO, RGO, AuNPs and AuNPs/RGO nanocomposites against MDA-MB-231 cell lines was analyzed by acridine orange (AO) and ethidium bromide (EB) fluorescent staining. Cancer cells were seeded into 6 well plates (1×10^4 cells/well) and incubated for 24 h at 37 °C. Then, GSP, GO, RGO, AuNPs and AuNPs/RGO nanocomposites were added (quantity as per obtained IC_{50} values) to the cells and incubated for 24 h. The plate was stained with the mixture of AO (100 µg mL^{-1}) and EB (100 µg mL^{-1}) for 30 min and the excess dye was washed with PBS twice. The stained cells were viewed under the fluorescence microscope to visualize the induction of apoptosis.

Statistical analysis: The software SPSS (version 18.0) was used for statistical analysis. All error bars represent the standard error (SEM) of six independent experiments (n = 6) unless otherwise stated. The values not sharing a common superscript (a, b, c, d, e and f) differ significantly at $p < 0.05$.

RESULTS AND DISCUSSION

UV-visible studies: The UV-visible spectral data illustrates the formation of RGO by the reduction potential of GSP and subsequent attachment of AuNPs on the RGO nanosheets. Fig. 1a displays the UV-visible spectra of GO, RGO, AuNPs and AuNPs/RGO nanocomposites. The GO exhibits two prominent absorption peaks at ~ 230 nm and a weak shoulder peak at ~ 300 nm, attributed to the π-π* transition of aromatic C=C

bonds and the n-π* transition C=O groups, respectively [38]. After functionalized with GSP, the characteristic aromatic C=C bonds at ~ 230 nm were red-shifted to ~ 280 nm. The C=O band at ~ 300 nm was found to be completely disappeared in the RGO, which suggests the well-extended electronic conjugation and restoration of sp^2 hybridized carbon arrangement within graphene sheets during the reduction process [35]. This apparent ~ 50 nm red shift indicates a high degree of GO reduction and the formation of RGO by the GSP treatment. The GSP acts as a potent reducing agent due to several readily electron-donating -OH groups [34]. Previously, the GSP has successfully been employed to synthesize silver and iron nanoparticles [39]. Furthermore, the synthesis of AuNPs was also carried out using a GSP and a HAuCl₄ aqueous solution. The colour of the solution changed from brown to ruby red confirmed the formation of AuNPs (Fig. 1b). In addition, the formation of gold nanoparticles (AuNPs) was also confirmed by the observation of a typical surface plasmon resonance (SPR peak) at 526 nm. Moreover, the UV-vis absorption spectra of AuNPs/RGO nanocomposites exhibit two distinct RGO and AuNPs absorption peaks at wavelengths of 280 nm and 526 nm. These results demonstrated that the reduction of HAuCl₄ to Au on RGO nanosheets results in the formation of AuNPs/RGO nanocomposites (Fig. 1a). The significant colour variation during the reductive synthesis of AuNPs and the RGO nanosheets was also observed in Fig. 1b.
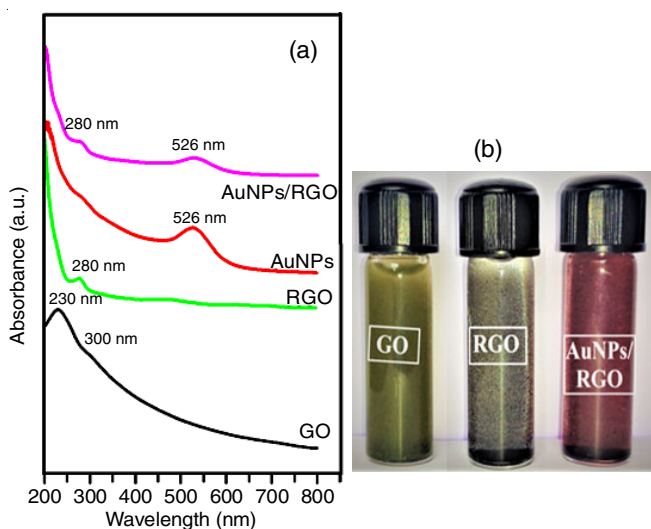

Fig. 1. (a) UV-Visible spectra for GO, RGO, AuNPs, AuNPs/RGO nanocomposites; (b) Photographs of aqueous suspension GO, RGO and AuNPs/RGO nanocomposites

FTIR studies: The FT-IR spectra of GO exhibit a broad characteristic band at 3426 cm⁻¹ which has been assigned to the O-H stretching vibration of adsorbed water molecules (Fig. 2). The peak at 1716 cm⁻¹ is ascribed to the C=O stretching vibration of carboxyl groups that exist on the edges of GO nanosheets. The band observed at 1625 cm⁻¹ is assigned to the C=C bonds that correspond to the skeletal vibration of unoxidized graphite domains. The band observed at 1384 cm⁻¹ and 1052 cm⁻¹ were attributed to the C–O stretching vibration of carboxyl
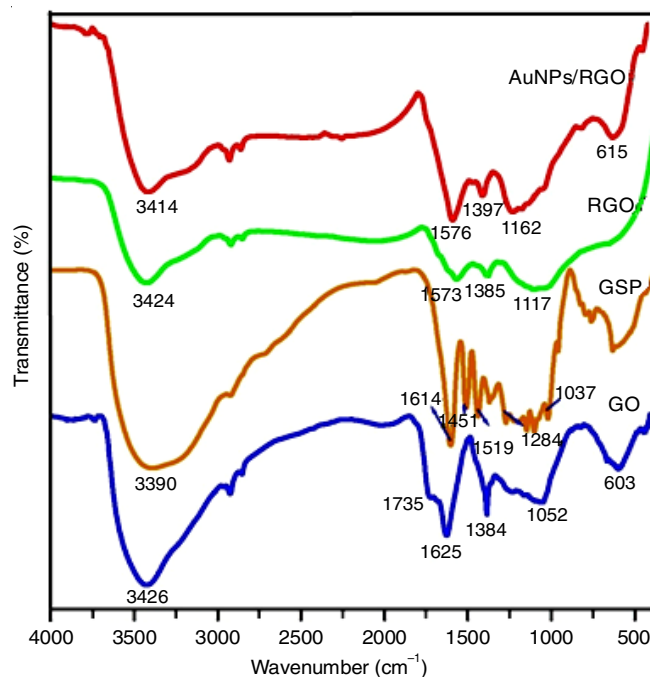

Fig. 2. FT-IR spectra of GO, GSP, RGO and AuNPs/RGO nanocomposites

and alkoxy groups, respectively. After reducing the GO by GSP, the characteristic C=O (at 1716 cm⁻¹) and C–O (at 1052 cm⁻¹) stretching vibrations of GO disappeared entirely in the RGO, indicating the removal of oxygen functionalities at the surface of GO [40]. Moreover, the FT-IR spectra of RGO revealed new bands at 1573 cm⁻¹ (skeletal C=C vibration) and 1117 cm⁻¹ (skeletal C–C stretching vibration) confirmed that GO was successfully exfoliated and reduced. However, the vibrational spectra of RGO at 3424, 1573, 1385 and 1117 cm⁻¹ were slightly shifted to 3414, 1576, 1397 and 1162 cm⁻¹ in the AuNPs/RGO nanocomposites, which confirms some minor chemical inter-action between AuNPs and RGO nanosheets through GSP reduction. Moreover, the new peak at 615 cm⁻¹ may correspond to the residual oxygen functional groups on the RGO sheet, which provide the active anchoring site for AuNPs by simple electrostatic attraction.

Morphology: The EDX analysis was conducted to confirm the presence of carbon, oxygen and metallic Au in the GSP functionalized AuNPs/RGO nanocomposites. The atomic and weight percentage of elements such as carbon, oxygen and gold that existed in the AuNPs/RGO nanocomposites are shown in the inset of Fig. 3. A sharp signal peak at 2.2 keV reveals the presence of metallic Au, which provides the substantial evidence for the successful decoration of AuNPs onto the surface of RGO nanosheets and are tightly bonded to each other. Moreover, it has been found that the AuNPs/RGO nanocomposites contain no traces of other elements or any other residues confirmed the high purity of the prepared nanocomposites.

The HR-TEM image of the developed biogenic RGO (Fig. 4) is typically transparent and thin multi-layered sheets with few wrinkles and smooth folded edges on its surface, these morphological features might be due to the intrinsic nature of RGO. It has been reported that 2D membrane structure would be thermodynamically stable *via* blending [41]. The low magn-

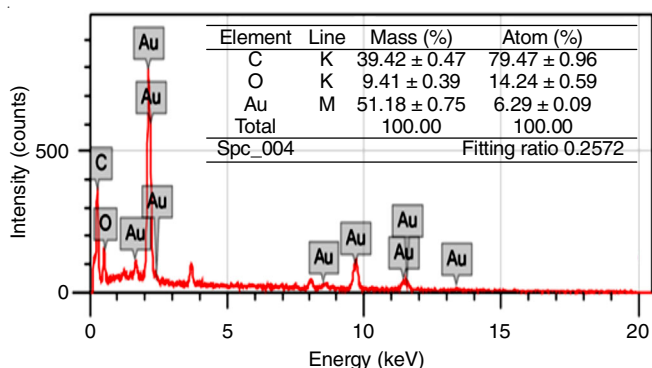| Element	Line	Mass (%)	Atom (%)
C	K	39.42 ± 0.47	79.47 ± 0.96
O	K	9.41 ± 0.39	14.24 ± 0.59
Au	M	51.18 ± 0.75	6.29 ± 0.09
Total		100.00	100.00
Spc_004			Fitting ratio 0.2572

Fig. 3. EDX spectra of AuNPs/RGO nanocomposites

ified HR-TEM micrograph (Fig. 4b) shows that the clear lattice fringes with an inter-planar spacing of 0.34 nm correspond to the (002) plane of RGO. This was presumably the removal of oxygen functional groups present in the GO sheets. Moreover, the HR-TEM image of AuNPs/RGO nanocomposites (Fig. 4c-d) shows that AuNPs have sphere-like morphology and are uniformly embedded on the surface of RGO nanosheets with slight agglomeration. Fig. 4d shows the inter-planar distance of 0.236 nm for AuNPs that corresponds to crystallographic planes (111) of metallic Au. The average size distribution of decorated AuNPs on the surface of the RGO nanosheets was found to be ~35 nm (Fig. 4e).

The zeta potential analysis was used to assess the surface charge and stability of the AuNPs/RGO nanocomposites. The value of zeta potential indicates the stability of synthesized GO, RGO and AuNPs/RGO nanocomposites (Fig. 5). The GO exhibits zeta potential value of -16.6 mV, which indicates the presence of density oxygen functional groups (carboxyl and epoxy) on the surface of the GO sheets. Further, RGO has more surface negative charge densities (-31.5 mV) than GO nanosheets. The zeta potential value of AuNPs/RGO nanocomposites exhibited a further higher negative zeta potential value -33.9 mV), which leads to a more stable dispersion in an aqueous solution [27]. This could be related to more electrostatic repulsive interaction between the negatively charged ions [42].

In vitro **cytotoxicity studies:** Dose-dependent inhibition of cell viability was observed during treatment with GSP, GO, RGO, AuNPs and AuNPs/RGO nanocomposites. The determined half-maximal inhibitory concentration (IC_{50}) values for GSP, GO, RGO, AuNPs and AuNPs/RGO nanocomposites were 1000, 62.5, 31.25, 31.25 and 15.6 µg/mL, respectively. The observed IC_{50} values indicate that the GSP alone did not exert any significant cytotoxicity against MDA-MB-231 cell lines. Further, treatment with GO alone exhibits lower cytotoxicity against MDA-MB- 231 than RGO, AuNPs and AuNPs/RGO nanocomposites. This was probably attributed to the rich oxygen atoms in carboxyl, epoxy and hydroxyl groups on the
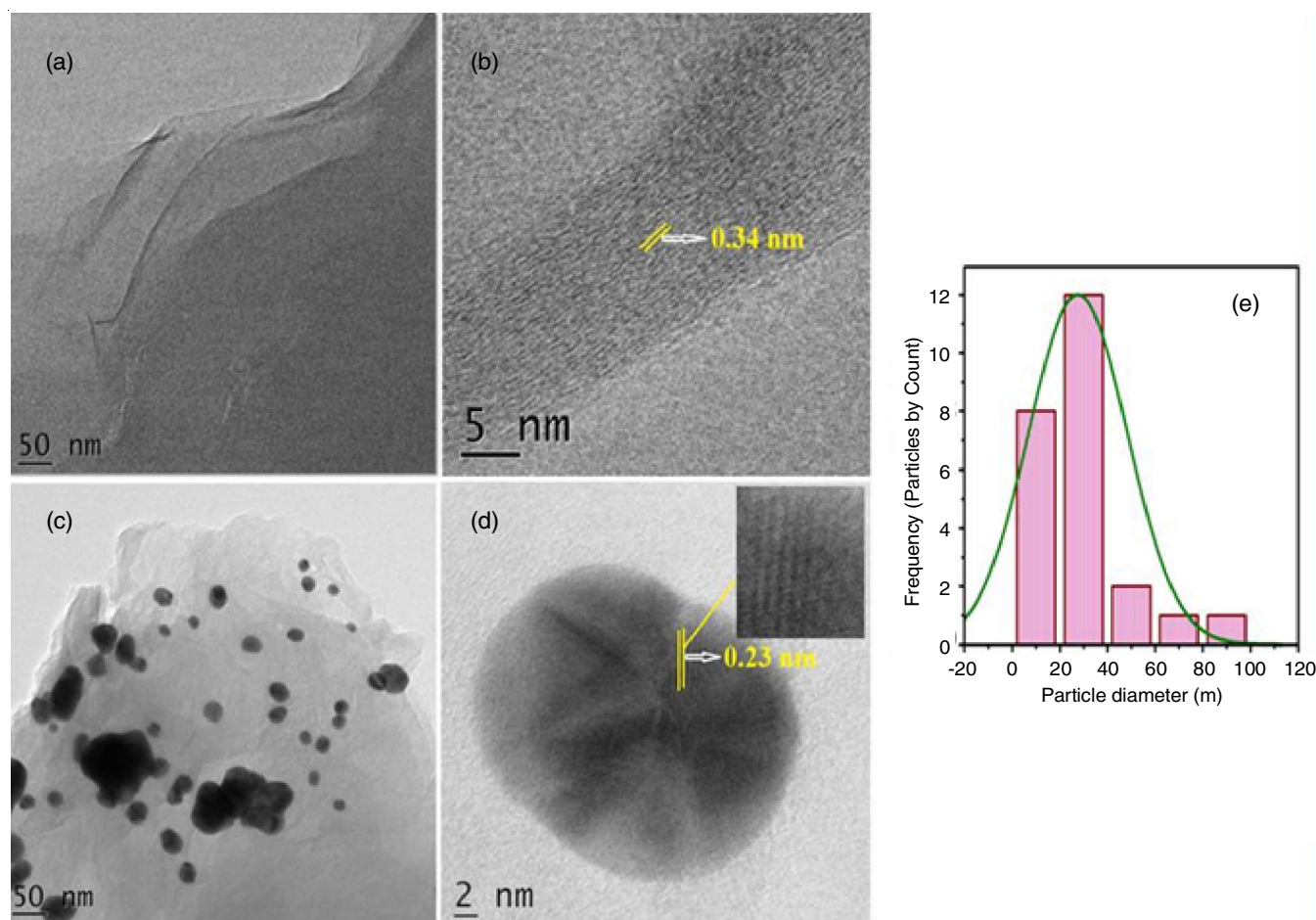

Fig. 4. HR-TEM image of (a and b) RGO nanosheets (c and d) AuNPs/RGO and (e) size distribution histogram
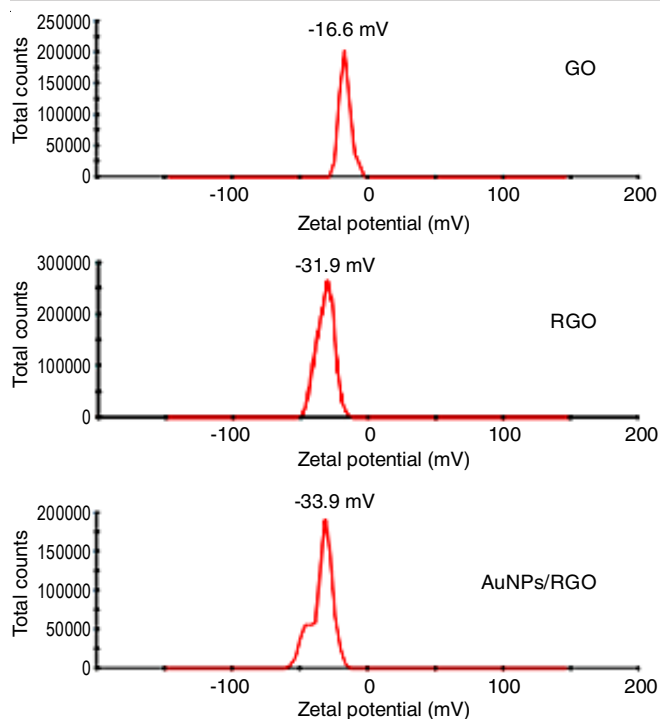
Fig. 5. Zeta potential distribution graph of synthesized GO, RGO and AuNPs/RGO nanocomposites
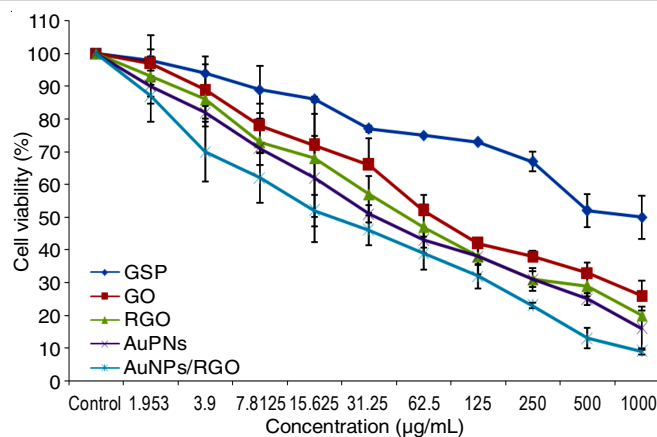

Fig. 6. MTT assay confirming the cytotoxicity of different concentrations of GSP, GO, RGO, AuNPs and AuNPs/RGO nanocomposites in MDA-MB-231 cell line after 24 h of treatment. The error bar represents the standard deviation of all samples for different doses (1.95-1000 µg/mL). The results were considered statistically significant if the *p*-value is less than 0.05

GO surface [43]. Interestingly, the IC_{50} (31.25 µg/mL) values of RGO and AuNPs were found to be similar to MDA-MB- 231 cell lines. Conversely, the IC_{50} value of AuNPs/RGO nanocomposites (15.6 µg/mL) was found to be lower than either RGO nanosheets or AuNPs alone treatment (Fig. 6). This result revealed that AuNPs/RGO nanocomposites have a greater cytotoxic effect against MDA-MB-231 cells than AuNPs and RGO nanosheets treatments individually. The observed enhanced anticancer potential of AuNPs/RGO nanocomposites was possibly due to the synergistic effect between the active sites of bioinspired AuNPs and the high specific surface area RGO. In addition, RGO plays a significant role in stabilizing AuNPs and preventing them from agglomeration to enhance the cytotoxicity in MDA-MB-231 cells. The results clearly demonstrated the enhanced cytotoxicity of AuNPs/RGO nanocomposites against MDA-MB-231 cell lines. This could be attributed to the intracellular delivery properties of RGO sheets and thereby, the cancer cells can accumulate plenty of well-dispersed spherical-shaped AuNPs. This could readily enhance the cell membrane penetration and effectively be delivered into targeted cancer cells mainly through their higher efficiency of endocytosis than AuNPs and RGO treatment alone, enhancing therapeutic performance. From the above results, it can be concluded that the synergistic effects of AuNPs/RGO nanocomposites exhibit pronounced anticancer activity than AuNPs and RGO treatment alone, even at low concentrations. The AuNPs/RGO nanocomposites synthesized using various biogenic approach also showed a synergistic therapeutic effect in tumor cells [27,44-46].

Detection of ROS generation: ROS plays a vital role in several physiological processes, including cell signaling and apoptosis, leading to oxidative cell damage [47]. Considerable bright green fluorescence intensity was observed in AuNPs/RGO nanocomposites which reveals more ROS generation when compared to RGO and AuNPs treatment alone. These results indicated that AuNPs/RGO nanocomposites can easily traverse the cell membrane barriers and enables more accumulation in the internal cell organelles due to their higher diffusion potential rate. It is known that excessive ROS generation results in free radical attack of membrane phospholipids, leading to a loss of cellular dysfunction and tissue damage [48]. This enhanced ROS level in MDA-MB-231 cells alters the mitochondrial activity and plays a significant role in apoptotic cell death (Fig. 7a-b).

Mitochondrial membrane potential (MMP, Δψm): The essential energy metabolism of mitochondria plays a vital role in regulating apoptosis. The deprivation of mitochondrial membrane potential (MMP, Δψm) was detected using lipophilic cationic Rhodamine-123. As seen from Fig. 8, the control cells, GSP and GO treated MDA-MB-231 cells emitted highly intense green fluorescence upon staining, indicating a polarized mitochondrial membrane potential. Conversely, cells treated with RGO, AuNPs and AuNPs/RGO nanocomposites exhibited weak green fluorescence upon staining, which leads to increased depolarization in MMP. This alteration is responsible for the loss in MMP and induced apoptotic cell death. On a comparative basis, the treatment with AuNPs/RGO nanocomposites had more invisible fluorescence upon staining, which further confirms the effective apoptosis in cancer cells through the mitochondria pathway. The central role of mitochondria for apoptotic cancer cell death during graphene based nanocomposites treatment has already been demonstrated [48,49].

Detection of apoptotic nuclei by EB/AO staining: Apoptosis is an essential physiologic process that plays a vital role in homeostasis. It can be characterized by various morphological and cellular changes such as chromatin condensation, membrane blebbing, cytoplasm shrinkage and DNA fragmentation [50]. The characteristic set of these changes remains the hallmarks of apoptosis since, it can be distinguished from viable, early or late apoptotic and necrotic cells using fluore-
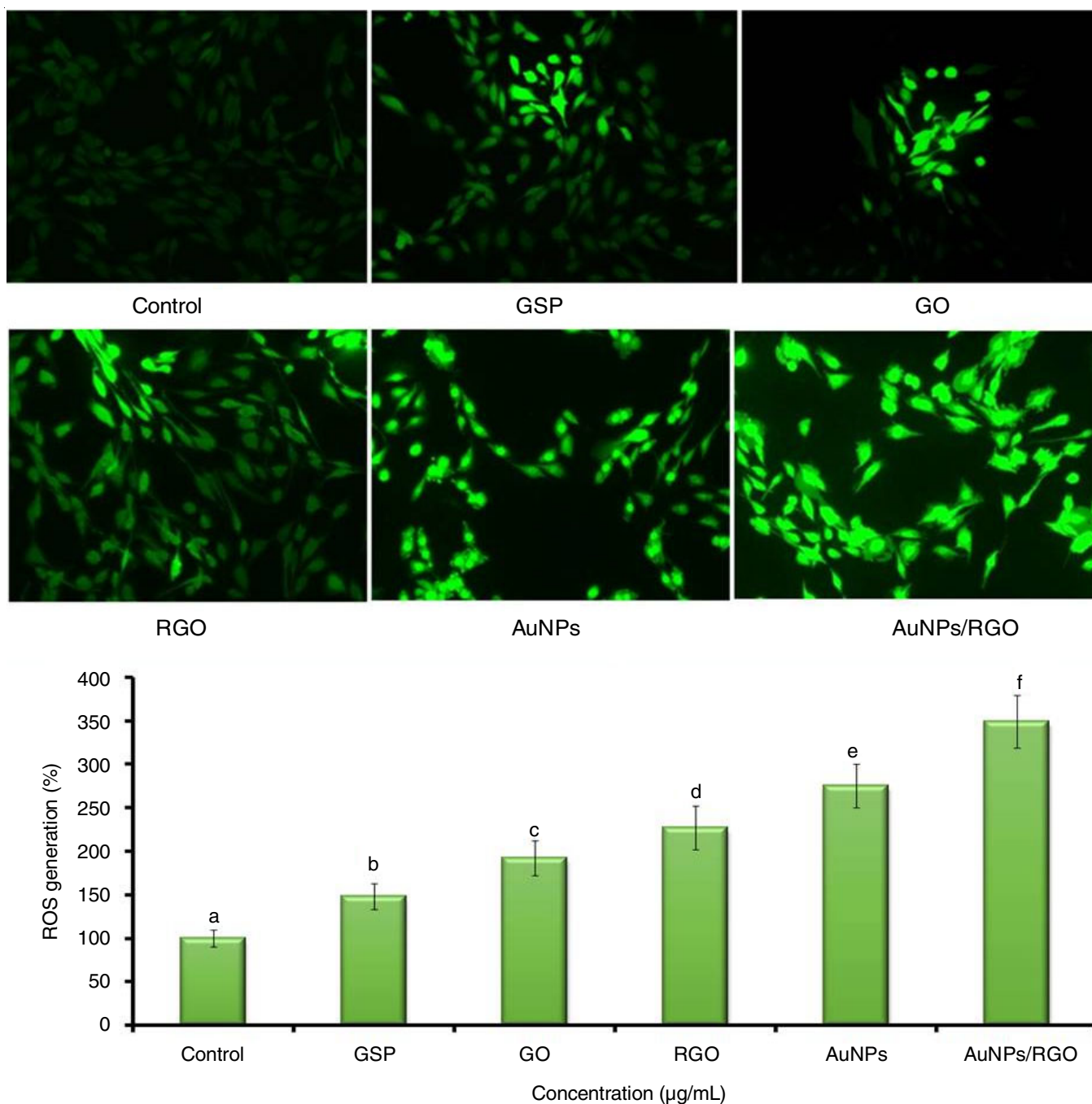
Fig. 7. (a) Fluorescence microscopy images of reactive oxygen species (ROS) generation in MDA-MB-231 cell line measurement by DCFH-DA staining; (b) Percentage ROS generation was calculated when compared to the control baseline ROS levels. Values are given as means ± SEM of six experiments in each group. Values not sharing a standard marking (a,b,c…) differ significantly at $p < 0.05$ (DMRT)

scence microscopy [51]. DNA binding fluorescent stains such as acridine orange/ethidium bromide (AO/EB) were used to determine any changes in intracellular nuclear morphology during cell death by apoptosis or necrosis [52]. AO can permeate the cell nucleus of both live and dead cells and emits green fluorescence if intercalated into DNA in viable cells and emits orange-red fluorescence if intercalated into DNA in non-viable cells. Conversely, EB is taken up only by dead cells upon inter-calating into DNA and emits red fluorescence when cytoplasmic membrane integrity is lost [53]. Fig. 9a shows the results of

dual staining apoptotic morphological changes MDA-MB-231 cells treated with GSP, GO, RGO, AuNPs and AuNPs/RGO nanocomposites treated MDA-MB-231cells. As seen in Fig. 9a, the control cells did not show any morphological changes with uniform fluoresced green nuclei and cytoplasm. Further, the number of apoptotic cells was increased after treatment with RGO and AuNPs alone (Fig. 9a-b). The AuNPs/RGO nano-composites showed significant alteration in the shape of cells, cytoplasm shrinkage, contracted nucleus and condensed chromatin, confirming the high occurrence of apoptosis in
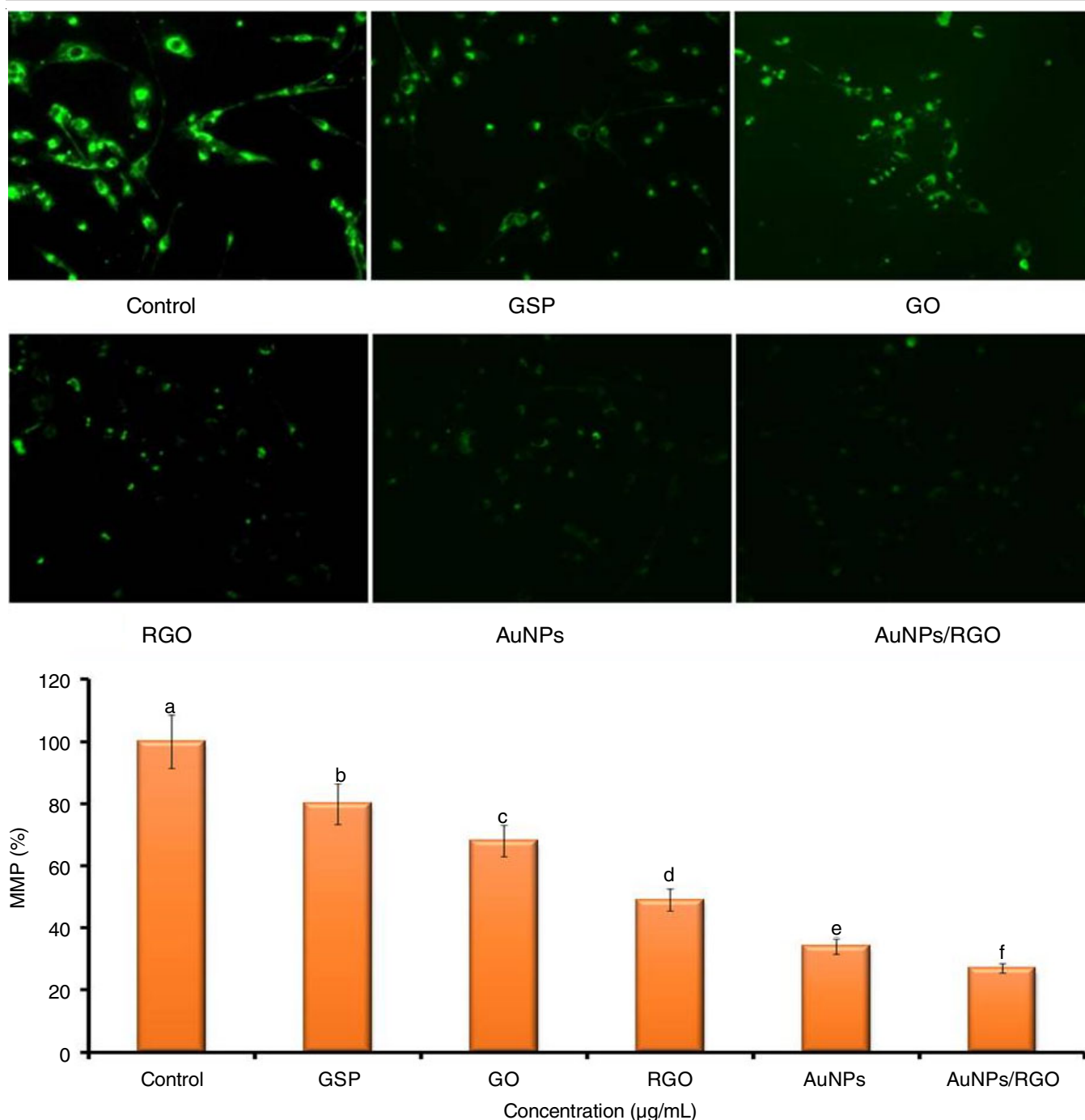
Fig. 8. (a) Fluorescence microscopy images of mitochondrial membrane potential and the morphological changes in MDA-MB-231 cell line using rhodamine-123 staining. (b) Fluorescence intensity was measured using a spectrofluorometer. Values are given as means ± SEM of six experiments in each group. Values not sharing a standard marking (a,b,c...) differ significantly at $p < 0.05$ (DMRT)

MDA-MB-231 cells. Moreover, the AO/EB staining results showed that the most robust red fluorescence (non-viable cells) was observed in AuNPs/RGO nanocomposites, which further confirm the high degree of apoptosis than the AuNPs and RGO alone.

Conclusion

In the present study, biogenic AuNPs/RGO nanocomposites have been developed using GSP as a reducing agent. The anal-

ytical techniques illustrated that spherical-shaped AuNPs with an average particle size of ~ 35 nm were uniformly decorated over the surface of transparent RGO nanosheets. These AuNPs/RGO nanocomposites exhibit synergistic anticancer effect through mitochondria mediated apoptotic cell death in triple-negative breast cancer cells. Therefore, the AuNPs/RGO nanocomposites may be considered potential anticancer agent that warrants preclinical animal experimentation to confirm their efficacy and toxicity profile.
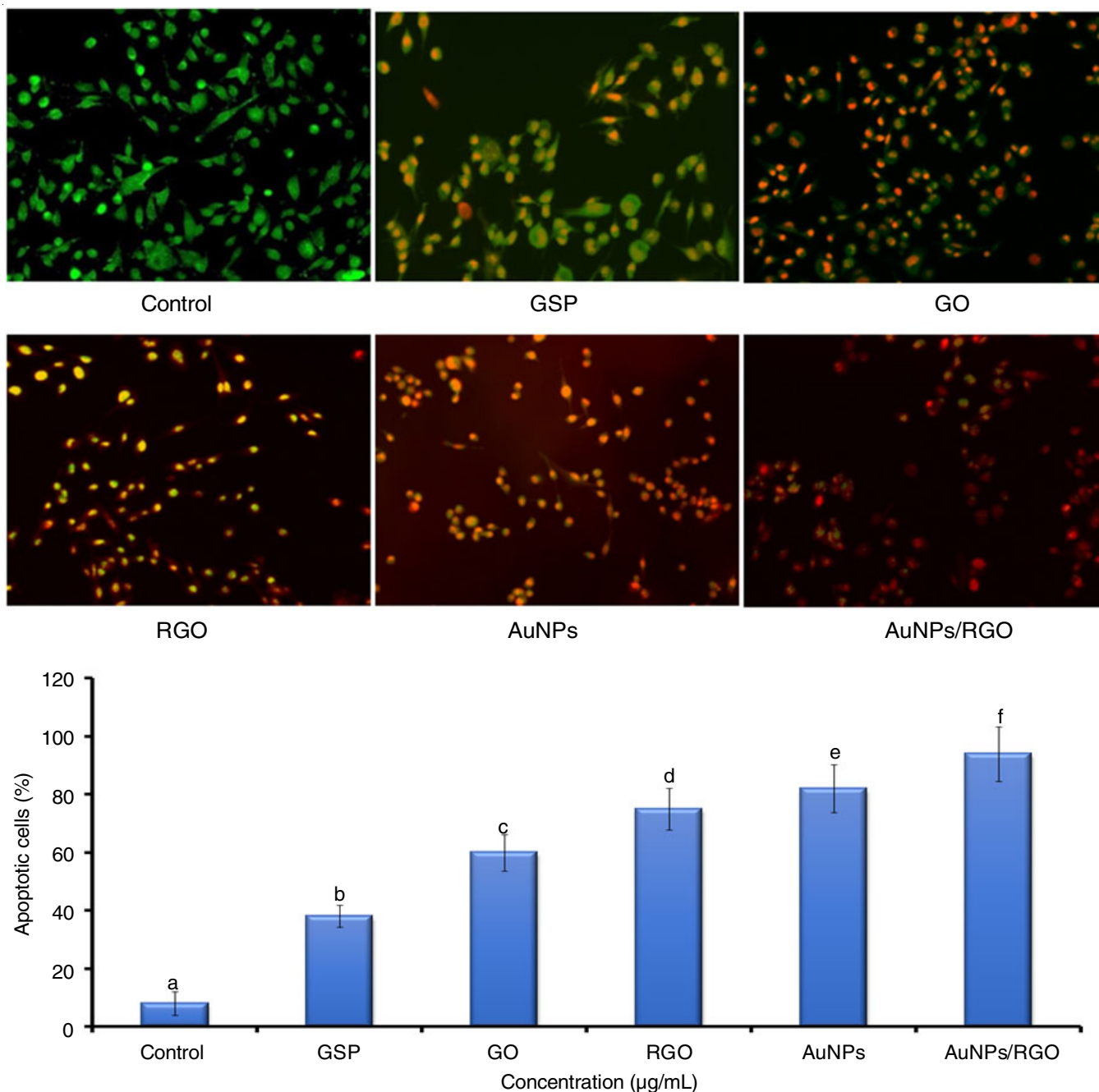
Fig. 9. (a) Fluorescence microscopy images of apoptosis-induced morphology of MDA- MB-231 cell line using AO/EB dual staining; (b) The scale bar represents the percentage of apoptotic cells. Values are given as means ± SEM of six experiments in each group. Values not sharing a standard marking (a,b,c…) differ significantly at $p < 0.05$ *vs.* control (DMRT)

CONFLICT OF INTEREST

The authors declare that there is no conflict of interests regarding the publication of this article.

REFERENCES

1. Z. Momenimovahed and H. Salehiniya, *Breast Cancer*, **11**, 151 (2019); https://doi.org/10.2147/BCTT.S176070
2. J. Sukumar, K. Gast, D. Quiroga, M. Lustberg and N. Williams, *Expert Rev. Anticancer Ther.*, **21**, 135 (2021); https://doi.org/10.1080/14737140.2021.1840984
3. P. Kumar and R. Aggarwal, *Arch. Gynecol. Obstet.*, **293**, 247 (2016); https://doi.org/10.1007/s00404-015-3859-y
4. Y. Zhao, E. Schaafsma and C. Cheng, *Cancer Med.*, **9**, 6281 (2020); https://doi.org/10.1002/cam4.3284
5. M. Mišík, M. Filipic, A. Nersesyan, M. Kundi, S. Knasmueller and M. Isidori, *Water Res.*, **164**, 114953 (2019); https://doi.org/10.1016/j.watres.2019.114953

6. T.M. Abu Samaan, M. Samec, A. Liskova, P. Kubatka and D. Büsselberg, *Biomolecules*, **9**, 789 (2019);
https://doi.org/10.3390/biom9120789

7. M. Lei, S. Sha, X. Wang, J. Wang, X. Du, H. Miao, H. Zhou, E. Bai, J. Shi and Y. Zhu, *RSC Adv.*, **9**, 5512 (2019);
https://doi.org/10.1039/C9RA00276F

8. Z. Yu, B. Yan, L. Gao, C. Dong, J. Zhong, M. D'Ortenzio, B. Nguyen, S. Seong Lee, X. Hu and F. Liang, *Curr. Cancer Drug Targets*, **16**, 509 (2016);
https://doi.org/10.2174/1568009616666151130213910

9. A. Shafei, W. El-Bakly, A. Sobhy, O. Wagdy, A. Reda, O. Aboelenin, A. Marzouk, K. El Habak, R. Mostafa, M.A. Ali and M. Ellithy, *Biomed. Pharmacother.*, **95**, 1209 (2017);
https://doi.org/10.1016/j.biopha.2017.09.059

10. S. Pasquali and A. Gronchi, *Ther. Adv. Med. Oncol.*, **9**, 415 (2017);
https://doi.org/10.1177/1758834017705588

11. S. Parvanian, S.M. Mostafavi and M. Aghashiri, *Sens. Biosensing Res.*, **13**, 81 (2017);
https://doi.org/10.1016/j.sbsr.2016.08.002

12. X. Wang and L. Cheng, *Nanoscale*, **11**, 15685 (2019);
https://doi.org/10.1039/C9NR04044G

13. L. Cheng, X. Wang, F. Gong, T. Liu and Z. Liu, *Adv. Mater.*, **32**, 1902333 (2020);
https://doi.org/10.1002/adma.201902333

14. Z. Mohammadpour and K. Majidzadeh-A, *ACS Biomater. Sci. Eng.*, **6**, 1852 (2020);
https://doi.org/10.1021/acsbiomaterials.9b01894

15. A.K. Geim and K.S. Novoselov, *Nature Mater.*, **6**, 183 (2007);
https://doi.org/10.1038/nmat1849

16. K. Yang, L. Feng, X. Shi and Z. Liu, *Chem. Soc. Rev.*, **42**, 530 (2013);
https://doi.org/10.1039/C2CS35342C

17. J. Byun, *J. Microbiol. Biotechnol.*, **25**, 145 (2015);
https://doi.org/10.4014/jmb.1412.12045

18. S. Pattnaik, K. Swain and Z. Lin, *J. Mater. Chem. B Mater. Biol. Med.*, **4**, 7813 (2016);
https://doi.org/10.1039/C6TB02086K

19. S. Priyadarsini, S. Mohanty, S. Mukherjee, S. Basu and M. Mishra, *J. Nanostructure Chem.*, **8**, 123 (2018);
https://doi.org/10.1007/s40097-018-0265-6

20. S. Song, H. Shen, Y. Wang, X. Chu, J. Xie, N. Zhou and J. Shen, *Colloids Surf. B Biointerfaces*, **185**, 110596 (2020);
https://doi.org/10.1016/j.colsurfb.2019.110596

21. G. Darabdhara, M.R. Das, S.P. Singh, A.K. Rengan, S. Szunerits and R. Boukherroub, *Adv. Colloid Interface Sci.*, **271**, 101991 (2019);
https://doi.org/10.1016/j.cis.2019.101991

22. S. Gurunathan, M. Jeyaraj, M.-H. Kang and J.-H. Kim, *Polymers*, **11**, 733 (2019);
https://doi.org/10.3390/polym11040733

23. R. Rajeswari and H.G. Prabu, *Process Biochem.*, **93**, 36 (2020);
https://doi.org/10.1016/j.procbio.2020.03.010

24. L.A. Al-Ani, M.A. AlSaadi, F.A. Kadir, N.M. Hashim, N.M. Julkapli and W.A. Yehye, *Eur. J. Med. Chem.*, **139**, 349 (2017);
https://doi.org/10.1016/j.ejmech.2017.07.036

25. I. Khan, K. Saeed and I. Khan, *Arab. J. Chem.*, **12**, 908 (2019);
https://doi.org/10.1016/j.arabjc.2017.05.011

26. V.S. Madamsetty, A. Mukherjee and S. Mukherjee, *Front. Pharmacol.*, **10**, 1264 (2019);
https://doi.org/10.3389/fphar.2019.01264

27. S. Gnanasekar, D. Balakrishnan, P. Seetharaman, P. Arivalagan, R. Chandrasekaran and S. Sivaperumal, *ACS Appl. Nano Mater.*, **3**, 4574 (2020);
https://doi.org/10.1021/acsanm.0c00630

28. R.G. Bai, K. Muthoosamy, F.N. Shipton, A. Pandikumar, N.M. Huang, P. Rameshkumar and S. Manickam, *RSC Adv.*, **6**, 36576 (2016);
https://doi.org/10.1039/C6RA02928K

29. G. Bhattacharya, S. Sas, S. Wadhwa, A. Mathur, J. McLaughlin and S.S. Roy, *RSC Adv.*, **7**, 26680 (2017);
https://doi.org/10.1039/C7RA02828H

30. E. Nagaraj, P. Shanmugam, K. Karuppannan, T. Chinnasamy and S. Venugopal, *New J. Chem.*, **44**, 2166 (2020);
https://doi.org/10.1039/C9NJ04961D

31. J.R. Peralta-Videa, Y. Huang, J.G. Parsons, L. Zhao, L. Lopez-Moreno, J.A. Hernandez-Viezcas and J.L. Gardea-Torresdey, *Nanotechnol. Environ. Eng.*, **4**, 1 (2016);
https://doi.org/10.1007/s41204-016-0004-5

32. R. Shanmuganathan, G. Sathishkumar, K. Brindhadevi and A. Pugazhendhi, *J. Mater. Res. Technol.*, **9**, 7013 (2020);
https://doi.org/10.1016/j.jmrt.2020.03.118

33. Y.-G. Yuan, Y.-H. Wang, H.-H. Xing and S. Gurunathan, *Int. J. Nanomedicine*, **12**, 5819 (2017);
https://doi.org/10.2147/IJN.S140605

34. N. Unusan, *J. Funct. Foods*, **67**, 103861 (2020);
https://doi.org/10.1016/j.jff.2020.103861

35. S. Sadhukhan, T.K. Ghosh, D. Rana, I. Roy, A. Bhattacharyya, G. Sarkar, M. Chakraborty and D. Chattopadhyay, *Mater. Res. Bull.*, **79**, 41 (2016);
https://doi.org/10.1016/j.materresbull.2016.02.039

36. T.A. Pham, J.S. Kim, J.S. Kim and Y.T. Jeong, *Colloids Surf. A Physicochem. Eng. Asp.*, **384**, 543 (2011);
https://doi.org/10.1016/j.colsurfa.2011.05.019

37. A. Sett, M. Gadewar, P. Sharma, M. Deka and U. Bora, *Adv. Nat. Sci. Nanosci. Nanotechnol.*, **7**, 25005 (2016);
https://doi.org/10.1088/2043-6262/7/2/025005

38. S.V. Otari, M. Kumar, M.Z. Anwar, N.D. Thorat, S.K.S. Patel, D. Lee, J.H. Lee, J.-K. Lee, Y.C. Kang and L. Zhang, *Sci. Rep.*, **7**, 10980 (2017);
https://doi.org/10.1038/s41598-017-10777-1

39. T. Toda, S. Hanesaka, K. Shishido, S. Fuji and H. Furuya, *J. Genet. Eng. Biotechnol.*, **18**, 1 (2020);
https://doi.org/10.1186/s43141-019-0015-2

40. J. An, G. Guo, R. Yin, Q. Luo, X. Li, F. Liu and D. Wang, *Polym. Int.*, **67**, 515 (2018);
https://doi.org/10.1002/pi.5537

41. Z. Wang, D. Xu, Y. Huang, Z. Wu, L. Wang and X. Zhang, *Chem. Commun.*, **48**, 976 (2012);
https://doi.org/10.1039/C2CC16239C

42. S. Fathalipour and E. Abdi, *Synth. Met.*, **221**, 159 (2016);
https://doi.org/10.1016/j.synthmet.2016.08.019

43. A. Jarosz, M. Skoda, I. Dudek and D. Szukiewicz, *Med. Cell. Longev.*, **2016**, 5851035 (2016);
https://doi.org/10.1155/2016/5851035

44. G. Chang, Y. Wang, B. Gong, Y. Xiao, Y. Chen, S. Wang, S. Li, F. Huang, Y. Shen and A. Xie, *ACS Appl. Mater. Interfaces*, **7**, 11246 (2015);
https://doi.org/10.1021/acsami.5b03907

45. N.K. Kadiyala, B.K. Mandal, S. Ranjan and N. Dasgupta, *Mater. Sci. Eng. C*, **93**, 191 (2018);
https://doi.org/10.1016/j.msec.2018.07.075

46. L.A. Al-Ani, W.A. Yehye, F.A. Kadir, N.M. Hashim, M.A. AlSaadi, N.M. Julkapli and V.K.S. Hsiao, *PLoS One*, **14**, e0216725 (2019);
https://doi.org/10.1371/journal.pone.0216725

47. M.F. Sanad, A.E. Shalan, S.M. Bazid, E.S. Abu Serea, E.M. Hashem, S. Nabih and M.A. Ahsan, *RSC Adv.*, **9**, 31021 (2019);
https://doi.org/10.1039/C9RA05669F

48. G. Rajivgandhi, M. Maruthupandy, F. Quero and W.-J. Li, *Sci. Eng. C.*, **102**, 829 (2019);
https://doi.org/10.1016/j.msec.2019.05.008

49. T. Kavinkumar, K. Varunkumar, V. Ravikumar and S. Manivannan, *J. Colloid Interface Sci.*, **505**, 1125 (2017);
https://doi.org/10.1016/j.jcis.2017.07.002

50. Y. Zhang, X. Chen, C. Gueydan and J. Han, *Cell Res.*, **28**, 9 (2018);
https://doi.org/10.1038/cr.2017.133

51. S. Elmore, *Toxicol. Pathol.*, **35**, 495 (2007);
https://doi.org/10.1080/01926230701320337

52. K. Liu, P. Liu, R. Liu and X. Wu, *Med. Sci. Monit. Basic Res.*, **21**, 253 (2015);
https://doi.org/10.12659/MSMBR.895463

53. S. Kasibhatla, G.P. Amarante-Mendes, D. Finucane, T. Brunner, E. Bossy-Wetzel and D.R. Green, *Cold Spring Harb. Protoc.*, **2006**, 4493 (2006);
https://doi.org/10.1101/pdb.prot4493